LA-UR- 98-2611



Title: Characterizing Mechanical Effects of Aging Damage

Author(s): Thomas D. Sewell, T-14
Shao-Ping Chen, T-11
Jon R. Schoonover, CST-4
Bruce C. Trent, X-NH
Philip M. Howe, DX-DO
Rex P. Hjelm, LANSCE-12
Richard V. Browning, ESA-EA

Submitted to: DOE OFFICE OF SCIENTIFIC AND TECHNICAL INFORMATION (OSTI)



**Los Alamos**
NATIONAL LABORATORY

## DISCLAIMER

# Characterizing Mechanical Effects of Aging Damage

Thomas D. Sewell[1], Shao-Ping Chen, Jon R. Schoonover, Bruce C. Trent, Philip M. Howe[2,3], Rex P. Hjelm[3] and Richard V. Browning[3]

## Abstract

This is the final report of a two-year, Laboratory Directed Research and Development (LDRD) project at the Los Alamos National Laboratory (LANL). Our goal was to develop and apply several different experimental and theoretical/computational tools to better understand physical and chemical aging phenomena in plastic-bonded high explosives, and to develop a methodology for predicting the likely effects of aging on the mechanical properties of the composite based on input from these fundamental studies. Initial comparisons were done for spectra of fresh and aged Estane, as well as PBX-9501, and we found differences in the carbonyl region of the spectrum, which possibly reflect differences in hydrogen bonding due to aging phenomena. The micromechanical model of composites was extended to study various volume fractions of "HMX" with "binders." The results showed that, as the binder fraction increases, there is a decrease in the maximum stress that can be supported but an increase in the percent strain at final fracture. A more realistic microstructural model was obtained through the use of a phase field model. Using this model, we have studied the microstructural evolution as a function of the grain boundary energy vs. misorientation relationship. The initial results indicate that there are some changes in the grain growth rate when the grain-boundary energy dependence on the angle is not constant. We also find that solute tends to segregate at the grain boundary and slows the grain growth kinetics.

## Background and Research Objectives

The goal of this work is to integrate experimental and theoretical/computational tools to identify, understand, and assess the effects of physical and chemical aging on the mechanical properties of filled composites. The material of primary interest in this project is PBX-9501, which is comprised of 95% by weight octahydro-1,3,5,7-tetranitro-1,3,5,7-tetrazocine (HMX) and 5% by weight polymeric binder; the latter is made up of 50% Estane 5703 and 50% BDNPA/F, plus a small percentage of Irganox. Estane 5703 is a

---

[1]Principal Investigator (PI) in second year of project, e-mail: sewell@lanl.gov

[2]PI in first year of project, e-mail: pmhowe@lanl.gov

[3]Participant in first year of project only

poly(ester-urethane) diblock copolymer, BDNPA/F is a nitroplasticizer, and Irganox is a radical scavernger. The chemical structure of Estane 5703 is

$-\{[O(CH_2)_4OOCNH(C_6H_4)CH_2(C_6H_4)NHCOO]_m-[(CH_2)_4OOC(CH_2)_4COO]_n\}-$,

where m=1-3 and n=4-6. The tools developed in this work are not specific to any particular material; the tools and methodology should be applicable to a wide range of organic composites.

The principal issues related to aging of PBX-9501 center around chemical degradation of the Estane by way of oxidative or hydrolytic pathways, leading to a decrease in molecular weight and migration of the nitroplasticizer under the small thermal gradient present in some applications. The concern is that if either of these possibilities proceeds too far, the mechanical properties of the binder may change, with the potential for concomitant changes in the mechanical properties and the ability to initiate the explosive. Clearly, this would be of interest with respect to the safety, performance, and reliability of weapons in the enduring nuclear stockpile. (To date, however, there is no evidence for such changes in the performance characteristics of PBX-9501.)

The multidisciplinary research performed under the auspices of this project combines a number of cutting-edge technologies including advanced spectroscopies and imaging tools, molecular dynamics simulation techniques, and mesoscopic simulation methodologies. Moreover, the approach employed requires the interplay of these tools to reach a successful conclusion. Finally, by definition, this work involves modeling of multiscale phenomena, which is an area of intense interest in connection with Science-Based Stockpile Stewardship (SBSS) due to the need to develop methods for using information obtained at one spatio-temporal scale and applying it to phenomena that occur at other, generally larger, ones.

## Importance to LANL's Science and Technology Base and National R&D Needs

The research performed in this project is applicable to several of the Laboratory core competencies, namely: complex experimentation and measurement; theory, modeling and high-performance computing; and nuclear weapons science and technology. The work, which has clear application to SBSS, is closely aligned with the Laboratory mission of reducing the global nuclear danger. Finally, each component of the work is of interest to U.S. commercial concerns, as evidenced by the continuation or extension of most aspects of the research *via* various industrial collaborations (described below).

## Scientific Approach and Accomplishments

### *Introduction*

Our approach is three-tiered. The first tier combines experimental characterization based on IR, Raman, and IV spectroscopies with results of classical molecular dynamics simulations (the latter being employed primarily as an interpretive tool for the former), for both fresh and aged materials. Spectroscopic data are obtained both for the actual composite and the constituents. These studies should enable us to discern what chemical and/or physical changes are occurring with time. Also, by using spatially resolved imaging tools, we should be able to identify behavior specific to interfacial regions. The second tier of the approach is to use molecular dynamics simulations to provide input needed for mesoscopic studies of the mechanical response to imposed strain. The principal quantities required of the molecular dynamics simulations are the elastic moduli of HMX and Estane, and the adhesion strength between them. In the third tier, the results of the mesoscale simulations are used to provide improved constitutive relations for use in a statistical mechanical, micro-mechanics-based approach to studying particle-filled composites.

### *Year One Accomplishments*

Standard operating procedures (SOPs) and shipping arrangements were put into place to allow for studies of explosive compositions. Spectroscopic investigations were performed on aged and fresh samples of bulk HE composite and pure binder material. The data indicated that changes had occurred, and it became clear that spatially resolved data were necessary for a better understanding of the aging process.

It was determined that a commercial software program (Biosym/MSI) would be the best tool for carrying out many of the atomistic theoretical studies. The code was delivered near the end of the first year of the project, and calculations of the material properties of Estane were undertaken.

Mesoscopic micro-mechanical studies based on the Potts spring network model were undertaken.

Progress was made in the development of a general constitutive theory for particle-filled composites. A computer model based on the discrete element method was constructed and shown to reproduce much of the characteristic behavior of such materials.

### *Year Two Accomplishments*

A Raman microscopy and imaging apparatus that uses 752-nm laser excitation was assembled. (Near infra-red light is needed for the experiments described here, as visible emission from organic complexes obscures the Raman spectra.) Work was also begun on testing an IR microscopy and imaging setup. Initial comparisons were done for spectra of

fresh and aged Estane, as well as PBX-9501. Based on these preliminary results, there are differences in the carbonyl region of the spectrum, which possibly reflect differences in hydrogen bonding due to aging phenomena.

Molecular dynamics and molecular mechanics simulations were used to compute the elastic constant matrix for the pure Estane polymer. Rigid molecule Monte Carlo simulations were used to compute the bulk modulus of HMX. Molecular dynamics calculations designed to study the interfacial (adhesion) dynamics of the Estane/HMX interface were planned for the third year of the project.

The micro-mechanical model of composites was extended to study various volume fractions of "HMX" with "binders". The results showed that, as the binder fraction increases, there is a decrease in the maximum stress that can be supported but an increase in the percent strain at final fracture. A more realistic microstructural model was obtained through the use of a phase field model.

***Industrial Collaborations***

This LDRD project has enabled us (Schoonover) to establish a collaboration with Patrick J. Treado from the University of Pittsburgh, president of ChemIcon Inc., and an internationally recognized leader in the development and application of Raman spectro-microscopy and imaging. His company has pioneered the use of liquid-crystal tunable filters in performing Raman imaging. We have generated some proof-of-principle data that has served as a basis for a proposal to study corrosion and aging issues using Raman imaging. The technology of ChemIcon, coupled with the technical problems and vibrational spectroscopy expertise here at Los Alamos, represent a potentially valuable collaborative effort.

We also established a collaboration with Richard A. Palmer at Duke University on the use of step-scan FTIR to (1) study the dynamic properties of polymer systems and (2) explore techniques to perform photo-acoustic depth profiling of PBX-9501. The idea is that spectral properties can change as a function of location of the sampling area of the HE. Finally, the spectroscopic work of Schoonover has been extended to two-dimensional FTIR studies, which allows for very incisive studies of the effects of external stresses (*e.g.*, stretching or temperature) on polymeric systems at the level of chemical functional groups.

The micro-mechanical modeling efforts of Chen have been included as part of a CRADA between Motorola and LANL. In addition, Molecular Simulations, Inc. is quite interested in the atomistic calculations performed by Sewell and discussions on possible collaborations are underway.

***Technical Vignettes from the Work***

In the following, we highlight in greater detail some of the work that was accomplished in this LDRD project.

*Spectroscopy of a Polyurethane Elastomer Under Thermal Stress - J. R. Schoonover*

Infrared spectroscopy has been used to study morphology, particularly changes in hydrogen bonding, in polyurethanes and polyurethane elastomers. This technique is useful because certain absorption bands characteristic of polyurethanes are influenced by the environment in which the polymer is located. Specifically, changes in hydrogen bonding can be observed through the N-H and C=O stretching regions of the spectrum. Hydrogen bonding is known to occur between the N-H group of the urethane segment and the C=O group of the urethane or ester segment, and is also known to decrease with an increase in temperature.

Several different types of polyurethanes have been studied by infrared spectroscopy. These types include poly(ether-urethanes) [**1-15**], poly(ester-urethanes) [**3, 16**], poly(urethane-urea)s [**17, 18**], and a simple polyurethane [**19**]. Srichatrapimuk and Cooper studied temperature-dependent behavior of poly(ether-urethane) and poly(ester-urethane) elastomers as a function of hard and soft segment lengths [**3**]. The IR absorptions in the N-H and C=O regions were monitored with temperature change to provide a quantitative measurement of phase separation. The enthalpy of hydrogen-bond dissociation was determined from the fraction of bonded groups at different temperatures. The H-bonded N-H stretch was located at 3320 cm-1, and the non-bonded N-H stretch was a shoulder at 3420 cm-1. The intensity of the bonded N-H stretch was observed to decrease, or shift to higher frequency, with an increase in temperature, indicating a decrease in hydrogen bonding. No splitting in the C=O region was observed in the poly(ester-urethanes). About 80% of N-H groups were calculated to be hydrogen-bonded at room temperature. More inter-urethane bonding occurred in polymers with longer hard and soft segments, and the hard-soft bonding was determined to dissociate first.

Siesler observed similar results to those of Srichatrapimuk and Cooper [**16**]. He conducted rheo-optical FTIR experiments of poly(ester-urethanes) at different temperatures by stretching and relaxation along a single axis. Temperature dependence of hydrogen bonding and structural organization of the hard segments were also studied. The change in the N-H region was attributed to a dissociation of hydrogen bonds and the small change in the C=O region was attributed to the functional group being less displaced. A shift of the N-H bending and C-N stretching band to lower frequency was observed, and was attributed to the inverse effect of hydrogen bonding on deformation vibrations.

The present work is a study of Estane 5703, a poly(ester-urethane) used as a structural support in industrial applications and as a binding agent in various high-explosive formulations. The relationship between the bulk properties and the molecular structure of estane are not well understood, and questions regarding the effects of aging of estane-based, high-explosive binding matrices have been difficult to answer. FTIR studies have been used to fundamentally relate molecular vibrations of estane, in its pure form at various temperatures, to its macroscopic structural and binding properties.

Experimental

Estane 5703, a polyurethane elastomer consisting of urethane hard segments and ester soft segments, was obtained from B.F. Goodrich. Samples were prepared by casting a dilute solution of the polymer onto 13-mm x 2-mm NaCl windows. Sample thickness was sufficient to yield an absorbance of under 1.5 absorbance units.

Samples were mounted between two NaCl windows in an aluminum block cell, which contained a cartridge heater and was connected to a temperature controller. The temperature was monitored through a Type K thermocouple placed next to the sample in the temperature cell. Temperature readouts were to an accuracy of 0.1 C. Spectra were taken with a Nicolet 20SXB FTIR spectrometer. Two hundred scans were measured with resolution of 8 $cm^{-1}$. Difference spectra were calculated by subtracting the spectrum at 100.0 C from the spectrum at 32.0 C.

Results And Discussion

Figure 1 is a spectrum of estane taken at 32.0 C. Table 1 summarizes the band assignments for this spectrum as made by Srichatrapimuk and Cooper [**3**]. The N-H region consists of two bands, one at 3340 $cm^{-1}$ representing hydrogen-bonded N-H stretching and the other at 3440 $cm^{-1}$ representing non-hydrogen-bonded N-H stretching.

The relative change in the N-H stretching region at 100.0 C is shown in Fig. 2. The difference spectrum shows a decrease in intensity of the bonded N-H stretch and an increase in intensity of the "free" N-H stretch. The N-H band is shifting to a higher intensity, indicating a decrease in hydrogen bonding.

The relative change in the C=O stretching region at 100.0 C is shown in Fig. 3. The difference spectrum shows three bands are changing in intensity. Hydrogen bonding between N-H of the urethane segment and C=O of both the urethane and ester segments must be decreasing. The overall band is shifting to a higher frequency with the measured temperature. The relative change in intensity, however, is small compared to the change for the N-H stretching region.

The relative changes in the N-H bending and C-N stretching regions are shown in Figs. 4 and Fig. 5, respectively. These bands are shifting to a lower frequency, due to the

inverse effect as noted by Siesler [**16**]. These relative changes are not small compared to the changes in the C=O stretching region.

Conclusion

Morphological changes in a poly(ester-urethane) were observed by infrared spectroscopy as changes in absorbance intensity of N-H, C=O, and C-N bands as a function of temperature. The N-H stretching and C=O stretching bands shifted towards higher frequency with an increase in temperature, while the two N-H bending and C-N stretching bands shifted towards lower frequency with an increase in temperature. Hydrogen bonding, both inter-urethane and hard-soft segment, decreases with temperature. The structural properties of estane, therefore, change with temperature. Two-dimensional cross-correlation analysis will next be applied to the spectra to resolve overlapped bands and to view related changes with temperature.

*Molecular Dynamics and Monte Carlo Calculations of the Mechanical Properties of β-HMX and Estane - T. D. Sewell*

The work described here is aimed towards developing a suite of tools and methods for predicting the equilibrium thermophysical properties of the constituents of plastic-bonded explosive formulations. Among the quantities of interest are crystal packing, density and bulk/linear coefficients of isothermal and isobaric expansion, specific heats, and mechanical properties based on the anisotropic elastic coefficient matrix. In the present work, the elastic moduli are of most interest. Here we describe calculations for β-HMX and Estane. These, along with BDNPA/F, are the major ingredients in PBX-9501.

Theoretical Methods

Our approach is statistical-mechanical, employing the numerical techniques of classical molecular dynamics and Monte Carlo, whereby the thermophysical properties follow from the interaction potential. Molecular dynamics using fully flexible molecules was used to calculate the mechanical properties of Estane, while rigid-molecule Monte Carlo was used to compute the hydrostatic compression properties of β-HMX.

*Estane*. Allen and Tildesley [**19**] provide a thorough description of the molecular dynamics methods used in the present work. All calculations were performed in the *NVT* ensemble, using the InsightII-based suite of programs from Molecular Simulations, Inc. As a first approximation to the actual structure of Estane, we formed diblock copolymer chains with hard and soft segments (defined above) in the ratio 2:5, with a total of 1202 atoms considered. All simulations were performed at the measured density, 1.18 g/cm$^3$; hence the edge length of the primary cell was approximately 24 Å on a side. Most of the calculations were performed using the PCFF force field [**20**], which has

been developed especially for use with polymeric systems. Initial chain configurations were generated using the Amorphous Cell program, based on the work of Theodoru and Suter [**21**]. The elastic constants for a given trajectory were obtained using the "static approach" described by Theodoru and Suter [**22**].

Briefly, starting with a cubic simulation box containing $N$ particles (a long chain, or several chains, folded into the primary simulation box) in a volume $V$, a long constant-temperature trajectory is computed to allow the system to relax to a representative equilibrium configuration. (It is assumed that the initial condition is close to a representative state since the relaxation time of polymer melts is far longer than can typically be simulated using atomistic molecular dynamics.) After the equilibration run has completed, an energy minimization is performed (still for constant volume and shape) to drive the system to a local minimum on the energy landscape. This energy-minimized configuration serves as the reference state for the system. The elastic stiffness coefficients $C_{lmnk}$ are obtained from numerical evaluation of the second derivatives,

$$C_{lmnk} = \left.\frac{\partial \sigma_{lm}}{\partial \varepsilon_{nk}}\right|_{\varepsilon_{nk}} = \left.\frac{1}{V^0}\frac{\partial^2 A}{\partial \varepsilon_{lm}\partial \varepsilon_{nk}}\right|_{\varepsilon_{lm},\varepsilon_{nk}} \approx \left.\frac{1}{V^0}\frac{\partial^2 U}{\partial \varepsilon_{lm}\partial \varepsilon_{nk}}\right|_{\varepsilon_{lm},\varepsilon_{nk}}, \qquad (1)$$

where $\sigma$ and $\varepsilon$ denote components of the stress and strain tensors, respectively, and $A$ and $U$ are the Helmholtz free energy and potential energy. The subscripts correspond to a set of twelve small deformations of the system (three pairs corresponding to uniaxial compression/tension, and three pairs corresponding to pure shear). Each deformation is performed and the energy re-minimized. The approximation indicated in Eq. 1 corresponds to neglecting the configurational entropy change on deformation. Although the static approach is computationally efficient, it suffers from the fact that the elastic constants are obtained from energy-minimized structures that essentially correspond to $T$=0 K. This will surely be reflected in the calculated moduli and Poisson's ratio. The procedures just described are performed for several different initial polymer configurations in the simulation box, and the results averaged. Since we are dealing with an isotropic system, the elastic coefficient matrix should be symmetric; this fact can be used to assess the statistical significance of the results.

An optional approach has been described by Brown and Clarke [**23**]. In their so-called dynamic approach, the calculation of moduli is obtained directly from the tensile strain and associated lateral contraction that results from imposition of an increasing uniaxial (tensile) stress on the system. In practice this is accomplished by performing constant stress dynamics for several time windows. The applied stress increases from one

window to the next. It is important to note that the routinely accessible strain rates used in molecular dynamics simulations are much higher than in experiments. Although this approach would have been a viable option for explicitly including the effects of finite temperature in our studies, in the following we consider only the static approach.

*β–HMX*. In isothermal-isobaric Monte Carlo [**24**], the macroscopic property $A(N,p,T)$ of a system of $N$ molecules at temperature $T$ and scalar pressure $p$ is obtained as an average of the microscopic function of configuration $A(\mathbf{q};V)$, the average taken over the states of a Markov chain in the $3N+1$ dimensional configuration space of the system,

$$A(N,p,T) = \lim_{M\to\infty} \frac{1}{M} \sum_{m=1}^{M} A(\mathbf{q}_m) , \tag{2}$$

in which the transition matrix between successive states is based on the potential energies $U_N(\mathbf{q}_m)$ and $U_N(\mathbf{q}_{m+1})$ of these states in such a way as to assure detailed balance and the equality of $A(N,p,T)$ with the actual ensemble average in the isothermal-isobaric ensemble,

$$\left\langle A_{NpT} \right\rangle = \frac{\int_0^\infty dV A e^{-\beta pV} Q(N,V,T)}{\int_0^\infty dV e^{-\beta pV} Q(N,V,T)}, \tag{3}$$

where $V$ denotes volume, $\beta=1/kT$, and

$$Q(N,V,T) = \int d\mathbf{q} e^{-\beta U_N(\mathbf{q})}. \tag{4}$$

In practice the averages are over a $6N+6$ dimensional space ($3N$ center-of-mass translations, $3N$ rotations about molecular centers of mass, and variations of the six variables required to specify the size and shape of the simulation cell) and attempted moves are evaluated using a Metropolis algorithm [**25**] in which trial moves are accepted or rejected according to $P=\min[\exp(-\Delta),1]$ where, for present state $m-1$ and "trial" state $m$,

$$\Delta = \beta\left\{\left[U(\mathbf{q}_m) - U(\mathbf{q}_{m-1})\right] + p(V_m - V_{m-1})\right\} - N\ln(V_m/V_{m-1}) \quad (5)$$

Maximum displacements were adjusted to yield roughly a 50% acceptance probability for a given kind of move. The battery of analyses described by Hald [**26**] was used to assess whether a particular realization was under statistical control.

The bulk was simulated by periodic replication in three dimensions of a primary simulation cell containing $N$ molecules. The replication was extended far enough into space to allow for all nonbonded interactions between molecules having centers of mass separated by less than 20Å.

The intermolecular potentials are of the form

$$U(\mathbf{R}) = \sum_{A\neq B}\sum_{i\in A}\sum_{j\in B}\left[U_{rep} + U_{disp} + U_{elec}\right], \quad (6)$$

where $A$ and $B$ are molecules, and $i$ and $j$ denote particular atoms. The repulsion and dispersion terms are written as

$$U_{rep} = A_{ij}e^{-B_{ij}R_{ij}} \quad \text{and} \quad U_{disp} = C_{ij}/R_{ij}^6, \quad (7)$$

respectively. The electrostatic contribution $U_{elec}$ to the intermolecular energy is

$$U_{elec} = q_i q_j / R_{ij}, \quad (8)$$

in which case potential-derived charges (PDQs) were used.

The nonbonded parameters $A_{ij}$, $B_{ij}$, and $C_{ij}$ for β-HMX were taken to be those reported by Williams [**27**]. Potential-derived atomic charges were obtained using the CHELPG method within the Gaussian 92 [**28**] suite of programs at the Hartree-Fock level using the 6-31g* basis set.

Results and Discussion

*Estane*. A set of fifteen independent configurations of the (assumed amorphous) Estane polymer were generated, using a total of 1202 atoms. At the prescribed density of 1.18 g/cm$^3$, this resulted in a simulation cell 25.4 Å on a side. Each configuration was allowed to equilibrate for 50 ps at a temperature $T$=300 K, after which the elastic constants were obtained by energy minimization using the static approach described by Theodoru and Suter [**22**]. The elements of the calculated elastic constant

matrix and their associated standard deviations are presented in Table 2. The resulting effective isotropic elastic moduli are presented in Table 3. The symmetry of the elastic constant matrix (Table 2) indicates reasonable convergence of the results, suggesting that the protocol used, fifteen independently generated and equilibrated configurations, is sufficient. The magnitudes of the elastic moduli (Table 3) are generally higher than expected for a rubbery material, and the Poisson's ratio lower than expected. This can be understood by realizing that the static approach corresponds to determination of the elastic constants at very low temperature, for which the material is in a glassy state and for which rubbery behavior would not be expected.

*β-HMX*. HMX exists in four different polymorphic forms. The stable structure at ambient temperature is known as β-HMX. It crystallizes in the monoclinic space group $P2_1/c$, with Z=2 molecules per unit cell [**29**]. The lattice parameters are $a$=6.54Å, $b$=11.05Å, $c$=8.70Å, and β=124.3 deg, yielding a density of ρ=1.894 g/cm$^3$. In this case, using a primary simulation cell containing only two perfectly rigid molecules (and using the measured unit cell as the initial geometry for our simulations), the calculated density at $T$=298K and $p$=1.00 bar is ρ=1.791(2) g/cm$^3$. Thus, our calculated "baseline" density for β-HMX is 5.4% too low.

Olinger *et al.* [**30**] performed an x-ray diffraction determination of the lattice parameters of β-HMX as a function of pressure (0.0 kbar ≤ $p$ ≤ 74.7 kbar), at a fixed temperature of $T$=293K. We have performed calculations for β-HMX over the same domain of pressures. The results are included in Table 4. In general, the results are in good agreement with experiment. The average percent errors compared to experiment for the lattice lengths $a$, $b$, and $c$ are 0.7%, 3.8%, and 1.0%, respectively. The general trends (not shown) with increasing pressure are: (1) decreasing errors for $a$ (2.0% → 0.0%); (2) increasing errors for $b$ (1.2% → 5.3%); and (3) decreasing errors for $c$ (2.7% → -0.4%).

Calculated results for the bulk compression of β-HMX are compared to experiment in Fig. 6, where we present the ratio $V/V^0$ of the unit cell volume at pressure $p$ to that at $p$=0. The results indicate fairly good agreement with experiment. By definition, the calculated and measured results are identical at $p$=0 kbar. At a pressure of 74.7 kbar, the calculated value of $V/V^0$ is in error by only -1.8% (i.e., slightly too compressible).

A limited assessment of possible finite-size effects was performed for the case $p$=40.3 kbar. Specifically, simulations were performed using $N$=2 molecules (the unit cell), $N$=4 molecules (three cases, each corresponding to a doubling of the unit cell along one of the lattice directions), and $N$=16 molecules (doubling the unit cell along each of the three lattice directions). Extrapolation of various calculated quantities plotted versus $1/N$ to the $y$ intercept indicated only minor size effects, *e.g.,* a 0.38% change in the density in passing from $N$=2 to $N$="$\infty$".

*Micromechanical Modeling of a PBX Using a Spring Network Model - S. P. Chen*

We have used a spring-network model to simulate the mechanical response of HMX + Binder composite systems. The starting configuration of the composite is "HMX" polycrystals with definite micro-structural grain-size distributions that have been generated by a Potts model simulation in a two-dimensional triangular grid of size from 150 by 150 to 700 by 700. The 'binder' was randomly distributed on the grids (see Fig. 7).

We have studied composites with binder concentrations ranging from 20% to 30%. The grids for HMX are connected by truncated harmonic oscillator springs that deform elastically until they break under extension at a predetermined value. The binder springs also deform elastically until they break, but with a much smaller elastic modulus compared to the "HMX" crystals. The value chosen for the ratio of elastic moduli, 1:100, approximates the experimental ratio.

The spring-network model indicates that, as the interface bonds are weakened (as might happen under aged conditions), the likelihood for intergranular or interfacial failure increases. This interfacial weakening promotes fracture along the grain boundaries (or interfaces), and provides nonlinear fracture paths for crack advancement. The studies for the 10% inclusion of binders show that as the volume fraction increases, there is a decrease in the maximum stress that can be achieved but an increase of strain before final fracture (see Fig. 8). As the volume fraction increases from 10% to 20% and to 30%, we find that the maximum stress decreases and failure occurs at more places in the composite and the stress-strain curves are less brittle-like.

On another front, we worked to incorporate the atomistic nature of the interface into the evolution of microstructures. By using a phase-field model, we have studied the microstructural evolution as a function of the grain boundary energy vs. misorientation relationship. The initial results indicate that there are some changes in the grain growth rate when the grain boundary energy dependence on the angle is not constant. We also find that solute tends to segregate to the grain boundary and slow the grain growth kinetics.

## Publications

1. Sewell, T. D, "Monte Carlo Calculations of the Hydrostatic Compression of RDX and β-HMX," J. Appl. Phys. (accepted).

2. Sewell, T. D., Kober, E. M., "Understanding the Physical and Mechanical Properties of Plastic-Bonded High Explosive Formulations," to appear in the February 1998 edition of: "Solutions" (Molecular Simulations, San Diego, 1998).

3. Sewell, T. D., "Monte Carlo Calculations of the Physical Properties of RDX, *b*-HMX, and TATB," to appear in Shock Compression of Condensed Matter-1997, edited by Schmidt, S. C., Dandekar, D. P., and Forbes, J. W. (AIP Press, New York, 1998).

4. Fan, D., Chen, L. Q, and Chen, S. P., "Numerical Simulation of Zener Pinning with Growing Second Phase Particles," J. Am. Ceram. Soc. (submitted).

5. Fan, D., Chen, L. Q., Chen, S. P., and Voorhees, P. W., "Phase Field Formulation for Modeling the Oswald Ripening in Two-Phase Systems," Computational Materials Science (in press).

6. Fan, D., Chen, S. P., and Chen, L. Q., "Computer Simulation of Grain Growth Kinetics with Solute Drag," J. Mat. Res. (submitted).

## References


1. Paik Sung, C. S.; Schneider, N. S., Macromolecules, **8**, 68 (1975).

2. Paik Sung, C. S.; Schneider, N. S., Macromolecules, **10**, 452 (1977).

3. Srichatrapimuk, V. W.: Cooper, S. L., J. Macromol. Sci., Phys., **B15**, 267 (1978).

4. Senich, G. A.; MacKnight, W. J., Macromolecules, **13**, 106 (1980).

5. Brunett, C. M.; Hsu, S. L.; MacKnight, W. J., Macromolecules, **15**, 71 (1982).

6. Christenson, C. P.; Harthcock, M. A.; Meadows, M. D.; Spell, H. L.; Howard, W. L.; Creswick, M. W.; Guerra, R. E.; Turner, R. B., J. Polym. Sci., Polym. Phys. Ed., **24**, 1401 (1986).

7. Koberstein, J. T.; Gancurz, I.; Clarke, T. C., J. Polym. Sci., Polym. Phys. Ed., **24**, 2487 (1986).

8. Lee, H. S.; Wang, Y. K.; Hsu, S. L., Macromolecules, **20**, 2089 (1987).

9. Coleman, M. M.; Skrovanek, D. J.; Hu, J.; Painter, P. C., Macromolecules, **21**, 59 (1988).

10. Meuse, C. W.; Yang, X.; Yang, D.; Hsu, S. L., Macromolecules, **25**, 925 (1992).

11. Hong, J. L.; Lillya, C. P.; Chien, J. C. W., Polymer, **33**, 4347 (1992).

12. Wang, F. C.; Feve, M.; Lam, T. M.; Pascault, J. P., J. Polym. Sci., Polym. Phys. Ed., **32**, 1305 (1994).

13. Lee, H. S.; Hsu, S. L., J. Polym. Sci., Polym. Phys. Ed., **32**, 2085 (1994).

14. Reynolds, N.; Spiess, H. W.; Hayen, H.; Nefzger, H.; Eisenbach, C. D., Macromol. Chem. Phys., **195**, 2855 (1994).

15. Goddard, R. J.; Cooper, S. L., Macromolecules, **28**, 1390 (1995).

16. Siesler, H. W., Polym. Bull., **9**, 471 (1983).

17. Bummer, P. M.; Knutson, K., Macromolecules, **23**, 4357 (1990).

18. Teo, L. S.; Chen, C. Y.; Kuo, J. F., Macromolecules, **30**, 1793 (1997).

19. Allen, M. P. and Tildesley, D. J., *Computer Simulation of Liquids* (Oxford Clarendon Press, Oxford, 1987).

20. Polymer 3.0.0 Polymer Modeling Software User Guide, October 1995 (San Diego, Biosym/MSI, 1995), Part 2, Chapter 18, p. 18-2.

21. Theodoru, D. N. and Suter U. W., Macromolecules **18**, 1467 (1985).

22. Theodoru, D. N. and Suter U. W., Macromolecules **19**, 139 (1986).

23. Brown, D. and Clarke, J. H. R., Macromolecules **24**, 2075 (1991).

24. Wood, W. W., in *Physics of Simple Fluids*, Temperley, H. N. V., Rowlinson, J. S., and Rushbrooke, G. S., Eds., Amsterdam: North-Holland, 1968, ch. 5, p. 115.

25. Metropolis, N., Rosenbluth, A. W., Rosenbluth, M. N., Teller, A. H., and Teller, E., J. Chem. Phys. **21**, 1087 (1953).

26. Hald, A., *Statistical Theory with Engineering Applications*, New York: John Wiley & Sons, 1952, ch. 13, p. 338.

27. Williams, D. E. and Cox, S. R., Acta Cryst. **B40**, 404 (1984); Cox, S. R., Hsu, L. Y., and Williams, D. E., Acta Cryst. **A37**, 293 (1981)

28. Gaussian92/DFT, Revision G.1, Frisch, M. J., Trucks, G. W., Schlegel, H. B., Gill, P. M. W., Johnson, B. G., Wong, M. W., Foresman, J. B., Robb, M. A., Head-Gordon, M., Replogle, E. S., Gomperts, R., Andres, J. L., Raghavachari,K., Binkley, J. S., Gonzalez, C., Martin, R. L., Fox, D. J., Defrees, D. J., Baker, J., Stewart, J. J. P., and Pople, J. A., Gaussian, Inc., Pittsburgh, PA, 1993.

29. Choi, C. S. and Boutin, H. P., Acta Cryst. **B26**, 1235 (1970).

30. Olinger, B., Roof, B., and Cady, H., "The Linear and Volume Compression of

β-HMX and RDX to 9 GPa (90 Kilobar)," presented at the Symposium International Sur le Comportement Des Milieux Denses Sous Hautes Pressions Dynamiques, Paris, France, 1978., p. 3.

Table 1. IR absorption band assignments for Estane 5703.

| Frequency ($cm^{-1}$) | Relative Intensity | Assignment |
|---|---|---|
| 3440 | weak, shoulder | free N-H stretch |
| 3340 | strong | bonded N-H stretch |
| 3190 | weak | cis-trans bonded N-H stretch |
| 3120 | weak | overtone of 1531 $cm^{-1}$ |
| 2951 | strong | $CH_2$ asymmetric stretch |
| 1732 | very strong | free and bonded C=O stretch in urethane and ester |
| 1597 | strong | C=C (benzene) stretch |
| 1531 | very strong | N-H bend/C-N stretch |
| 1415 | strong | C-C(benzene) stretch |
| 1315 | strong | N-H bend, C-N stretch, C-H bend |
| 1223 | strong | N-H bend/C-N stretch |
| 1180 | strong | C-O-C (ester) stretch |
| 1068 | strong | C-O-C (hard) stretch |

Table 2. Calculated elastic constant matrix for Estane. Standard deviations are in parentheses. Units are GPa.

| | | | | | |
|---|---|---|---|---|---|
| 12.6 (2.1) | 5.9 (1.9) | 6.2 (1.7) | 0.2 (1.8) | -0.1 (1.9) | -0.7 (1.3) |
| 5.8 (2.3) | 11.6 (3.0) | 6.4 (1.8) | 0.1 (1.4) | 0.6 (1.6) | 0.7 (2.0) |
| 6.7 (1.4) | 6.1 (2.2) | 14.1 (3.5) | -0.1 (1.6) | 1.1 (1.7) | -0.5 (1.9) |
| -0.5 (0.9) | -0.2 (1.6) | -0.3 (1.1) | 2.7 (1.5) | -0.5 (1.6) | 0.3 (1.2) |
| 0.1 (0.7) | -0.1 (0.8) | 0.4 (1.3) | -0.1 (0.8) | 3.2 (1.3) | -0.6 (0.9) |
| -0.5 (1.0) | -0.6 (1.3) | 0.0 (1.3) | -0.2 (1.0) | -0.7 (1.1) | 3.3 (1.3) |

Table 3. Calculated effective isotropic elastic moduli (GPa) and Poisson's ratio for Estane.\

| Type of Modulus | Value |
|---|---|
| Tensile | 8.794 |
| Bulk | 8.378 |
| Shear | 3.318 |
| Poisson's Ratio | 0.3251 |

Table 4. Calculated lattice parameters and unit cell volume for β-HMX. Uncertainties in the last reported digit are included in parentheses. Units are GPa, Å, degrees, and Å$^3$.

| Pressure | *a* | *b* | c | *β* | Volume |
|---|---|---|---|---|---|
| 0.00 | 6.674(7) | 11.17 (1) | 8.95 (1) | 124.5 (1) | 549.3(6) |
| 0.50 | 6.592(3) | 11.044(9) | 8.895(7) | 125.38(9) | 527.3(4) |
| 1.00 | 6.529(4) | 10.964(7) | 8.836(7) | 125.71(8) | 513.1(3) |
| 1.61 | 6.472(4) | 10.885(6) | 8.785(6) | 126.00(6) | 500.2(3) |
| 2.47 | 6.414(3) | 10.807(5) | 8.705(6) | 126.15(6) | 486.9(2) |
| 3.24 | 6.366(3) | 10.745(5) | 8.659(6) | 126.16(7) | 477.8(2) |
| 4.03 | 6.327(3) | 10.690(7) | 8.613(5) | 126.15(6) | 470.1(2) |
| 4.82 | 6.294(3) | 10.643(7) | 8.563(6) | 126.13(5) | 463.1(2) |
| 5.42 | 6.274(3) | 10.610(6) | 8.543(5) | 126.13(5) | 459.1(2) |
| 6.31 | 6.241(3) | 10.567(5) | 8.500(5) | 126.07(5) | 452.9(2) |
| 6.74 | 6.226(3) | 10.547(5) | 8.484(3) | 126.03(5) | 450.3(1) |
| 7.47 | 6.208(3) | 10.509(7) | 8.459(5) | 126.03(5) | 446.1(2) |

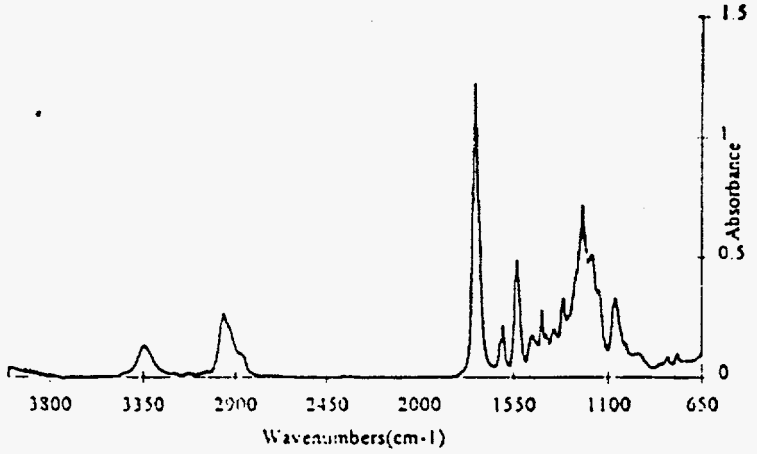


Figure 1. Infrared absorption spectrum of Estane at 32.0 C.

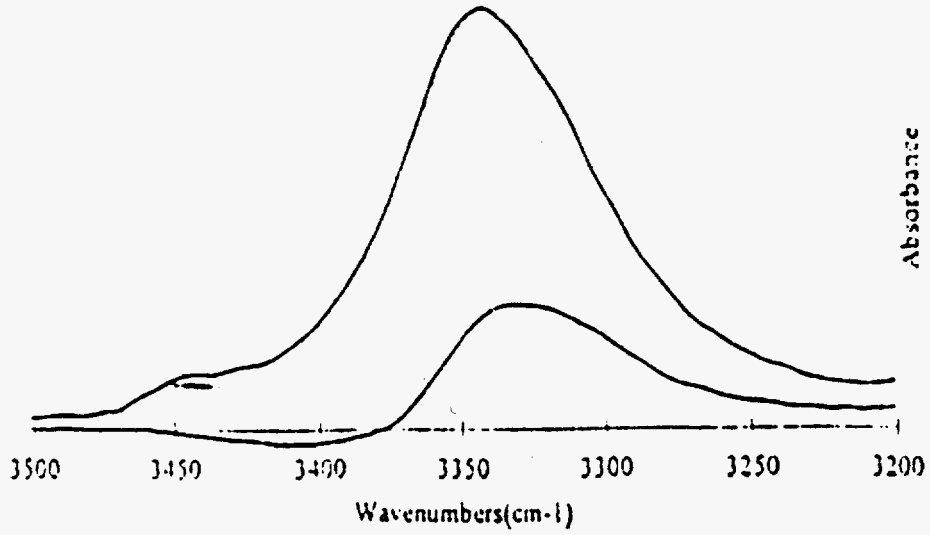


Figure 2. Relative change in the N-H stretching region at 100.0 C.

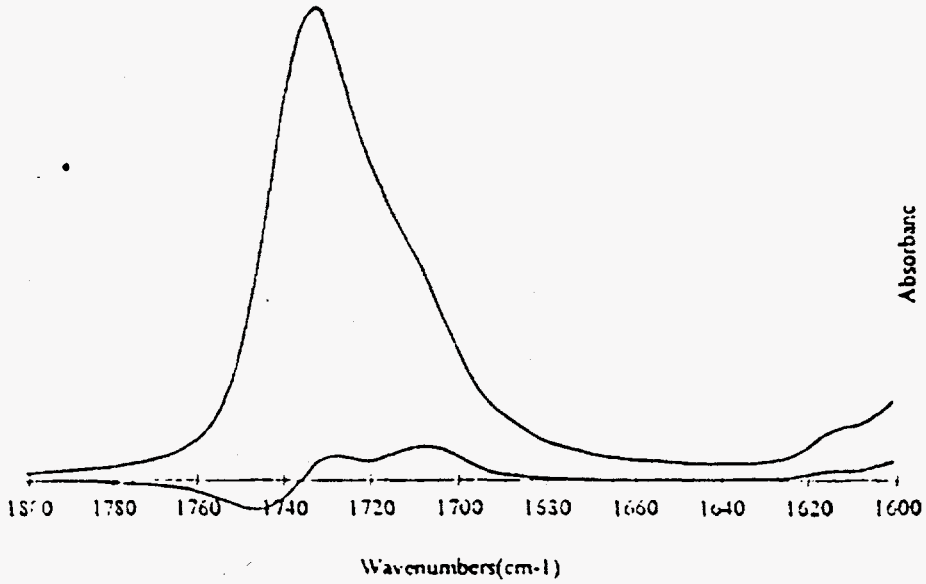


Figure 3. Relative change in the C=O stretching region at 100.0 C.

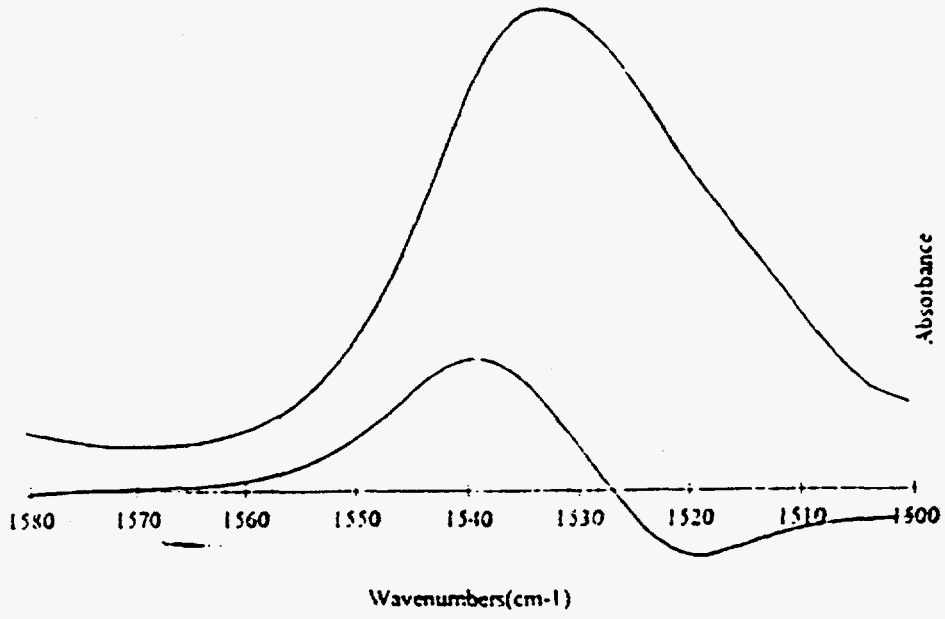


Figure 4. Relative band change in higher-frequency N-H bending and C-N stretching region at 100.0 C.

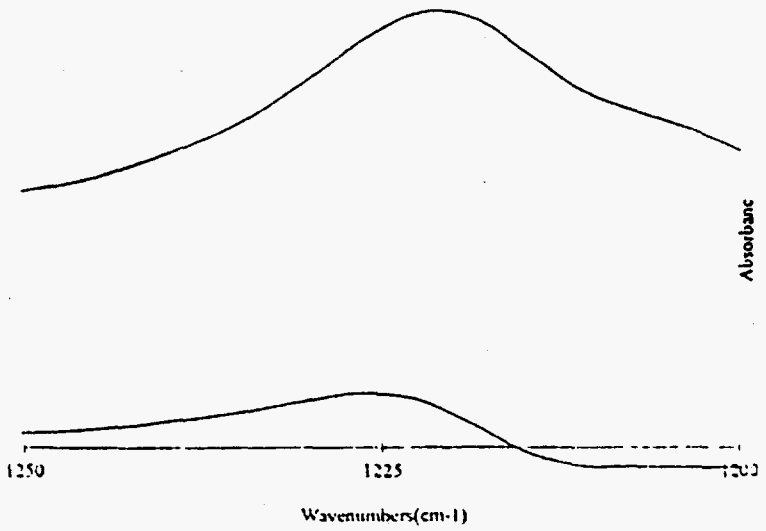


Figure 5. Relative band changes in the lower-frequency N-H bending and C-N stretching region at 100.0 C.

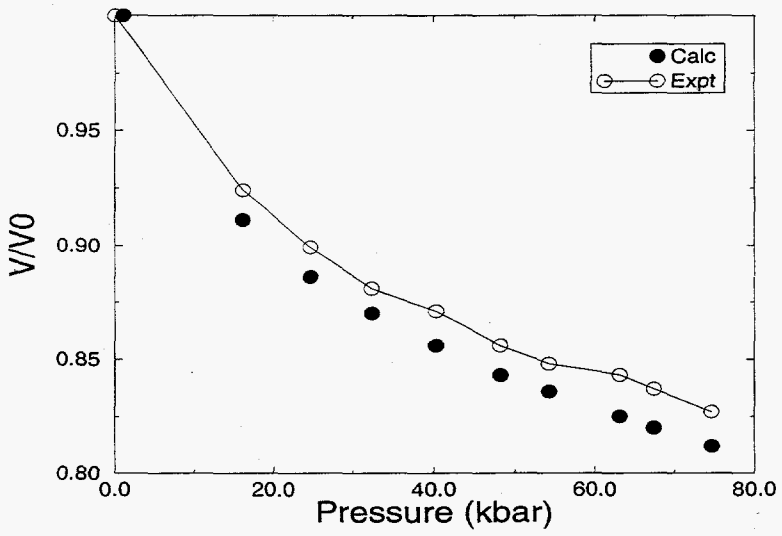


Figure 6. The bulk compression of β-HMX as a function of pressure is shown. $V/V^0$ is the ratio of the unit cell volume at pressure $p$ to that at $p$=0. Filled symbols: calculated results; open symbols: experiment.

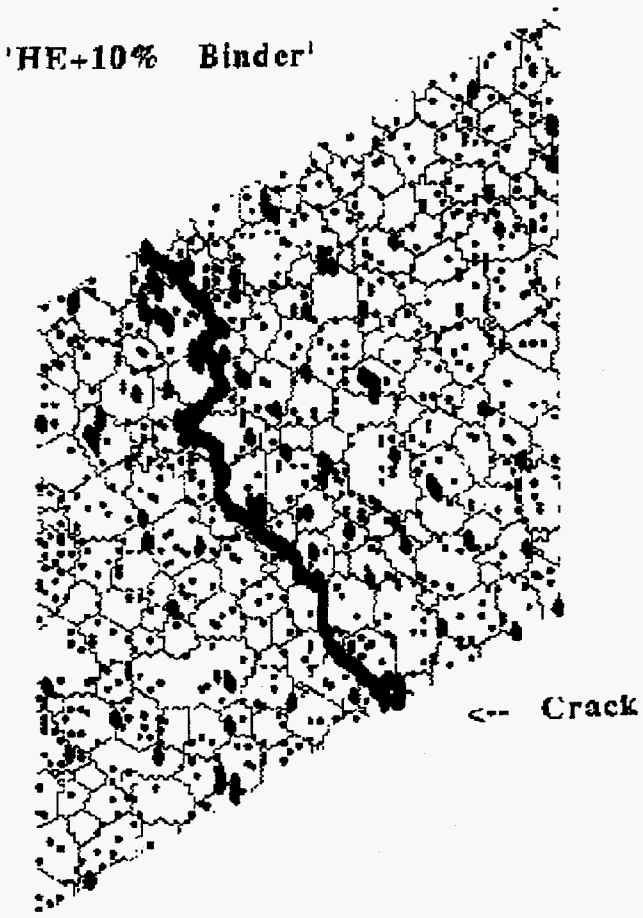


Figure 7. The computational model used to describe the mesoscale fracture of a PBX-9501-like composite is depicted. The "binder" is randomly distributed in the material.

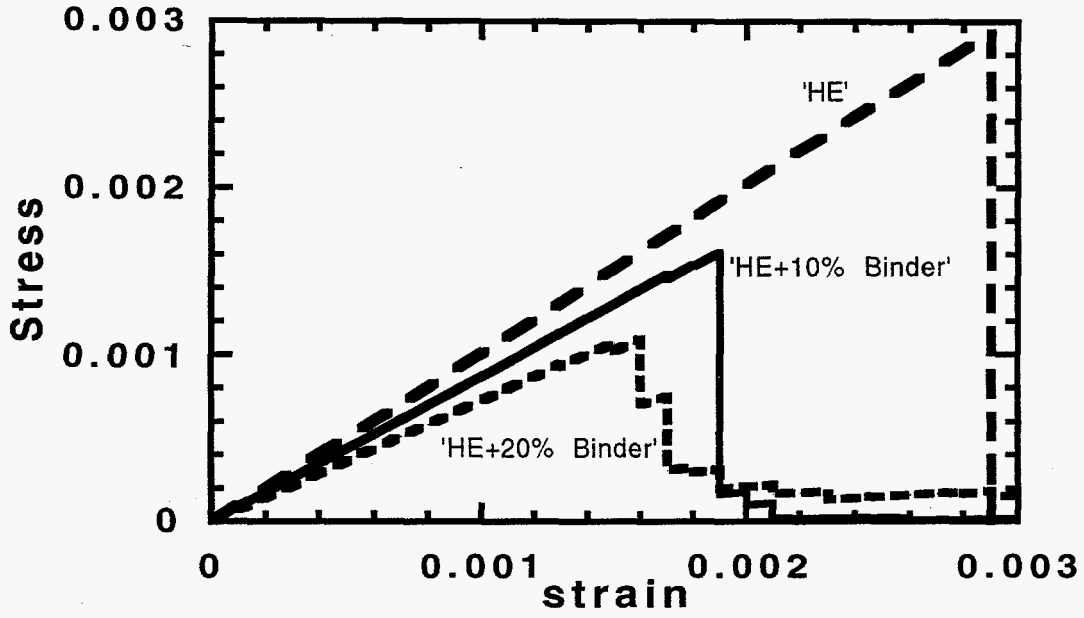


Figure 8. Calculated stress-strain curves as a function of "binder" concentration for the mesoscale model of PBX-9501.